

# Homogenization of an Electrophysiological Model for a Strand of Cardiac Myocytes with Gap-Junctional and Electric-Field Coupling

Paul E. Hand\*, Charles S. Peskin

*Courant Institute of Mathematical Sciences, New York University, New York, USA*

Received: 15 April 2009 / Accepted: 10 December 2009 / Published online: 5 January 2010  
© Society for Mathematical Biology 2010

**Abstract** We derive a homogenized description of the electrical communication along a single strand of myocytes in the presence of gap-junctional and electric-field coupling. In the model, cells are electrically coupled through narrow clefts that are resistively connected to extracellular space. Cells are also coupled directly through gap junctions. We perform numerical simulations of this full model and its homogenization. We observe that the full and homogenized descriptions agree when gap-junctional coupling is at physiologically normal levels. When gap-junctional coupling is low, the two descriptions disagree. In this case, only the full model captures the behavior that the ephaptic mechanism can speed up action potential propagation. A strength of our homogenized description is that it is a macroscale model that can account for the preferential localization of  $\text{Na}^+$  channels at the ends of cells.

**Keywords** Homogenization · Ephaptic · Syncytium · Electric field mechanism · Cardiac modeling · Gap junction

## 1. Introduction

Heart cells communicate electrically to coordinate the muscular contraction that pumps blood. Ions, such as  $\text{Na}^+$ ,  $\text{K}^+$ , and  $\text{Ca}^{2+}$ , pass in and out of cells through specialized channels, eventually causing a release of  $\text{Ca}^{2+}$  that initiates contraction. It is well accepted that gap junctions provide the primary conduit for electrical communication between myocytes (Rohr, 2004).

There is some evidence, though, that gap junctions do not tell the complete story of cellular coupling during action potential propagation in the heart. Hearts of lower vertebrates lack gap junctions yet still exhibit chains of electrical excitation (Sperelakis and McConnell, 2002). Additionally, a gene knockout study revealed that Connexin-43 deficient mice still have cardiac conduction, albeit at a reduced speed (Gutstein et al., 2001).

---

\*Corresponding author.

E-mail address: [hand@cims.nyu.edu](mailto:hand@cims.nyu.edu) (Paul E. Hand).

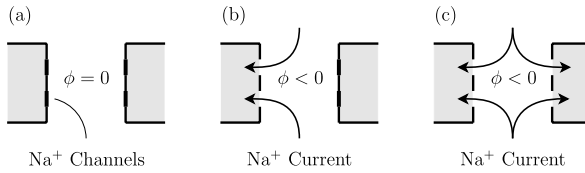


**Fig. 1** A cartoon of the electric-field mechanism between two adjacent cells (shaded). Initially, the  $\text{Na}^+$  channels of both the prejunctional (left) and post-junctional (right) cells are closed (a). When an action potential reaches the left cell, its  $\text{Na}^+$  channels open, allowing a flux of  $\text{Na}^+$  current in from extracellular space via the cleft (b). As per Ohm's law, the potential inside the cleft decreases, resulting in the depolarization of the post-junctional membrane. If this effect is sufficiently strong, the post-junctional membrane potential may reach threshold, causing the  $\text{Na}^+$  channels to open and allowing current to flow inward (c), thus initiating an action potential in the post-junctional cell.

A final observation suggesting that gap junctions are not the exclusive mechanism of cardiac electrical communication is the preferential localization to intercalated disks of  $\text{Na}^+$  channels in rat ventricular myocytes (Kucera et al., 2002). It is counterintuitive that the major depolarizing current would be located near the clefts, which are subject both to a high resistance to extracellular space and to potentially large fluctuations in ion concentrations. One might then suspect that the  $\text{Na}^+$  channel localization serves some purpose, perhaps as an aid to conduction.

Each of these observations suggests the existence of an electrical communication mechanism not mediated by gap junctions. Sperelakis and McConnell (2002) detail several possibilities including capacitive coupling, the electric-field mechanism, and ion accumulation. We focus on the electric-field mechanism, which is depicted in Fig. 1. In this mechanism, the inward  $\text{Na}^+$  current of the activated prejunctional membrane produces a cleft potential below that of extracellular space. This lowered cleft potential can then depolarize the post-junctional membrane, initiating an action potential in the post-junctional cell. This mechanism was first seen in a mathematical model of two cells by Sperelakis and Mann (1977), in which they observed that the effect requires the membranes at the ends of cells to be more excitable than at the sides of cells. The model was further extended to longer strands of cells in Picone et al. (1991) and with gap junctions in Ramasamy and Sperelakis (2007). The electric-field mechanism is also referred to as ephaptic coupling by Mori et al. (2008) and Copene and Keener (2008).

Kucera et al. (2002) also study action potential propagation along a strand of discrete cells with active membranes, coupled by gap junctions and a cleft potential. In their model, current can flow into and out of the cleft by a resistive connection to grounded extracellular space. Their model does not take into account effects of changes in ion concentration. Their numerical simulations show that the electric-field coupling can act to speed up conduction velocity relative to analogous models without the mechanism. In order to see this effect, though,  $\text{Na}^+$  channels must be localized to the intercalated disks at the ends of cells, and gap junction expression levels must be significantly reduced from their physiologically normal values. Their simulations also show that under normal gap junctional coupling, the electric-field mechanism acts to slow conduction.

Mori et al. (2008) show similar results with three-dimensional axisymmetric models that account for ion concentration effects within clefts. With normal gap junction expression, relocating  $\text{Na}^+$  channels to the intercalated disks can slow conduction if the clefts

are sufficiently narrow. These authors also describe a new mode of cardiac communication in which the electric-field and gap-junctional mechanisms alternate as the principal means of communication across successive junctions.

In the present paper, we derive a simplified partial differential equation (PDE) for electric-field coupling in the presence of gap junctions. The microscopic description that we take as our starting point is almost identical to the model in Kucera et al. (2002). We perform the mathematical process known as homogenization (Evans, 2002; Hornung, 1997), which involves introducing slow and fast independent spatial variables and performing a perturbation analysis. We then investigate numerically how well the homogenized model captures the electric-field effects described in Kucera et al. (2002). We detail the dependence of conduction velocity on gap junctional coupling,  $\text{Na}^+$  channel localization, and cleft-to-ground resistance. We observe that the homogenized and full descriptions of the electric-field mechanism agree well when gap junctions are present at physiologically normal levels, regardless of the partition of  $\text{Na}^+$  channels between the ends and the sides of cells. The homogenized and full descriptions disagree, however, when gap junctional levels are substantially below normal.

The remainder of the present paper is organized as follows. In Section 2, we detail a microscopic model that includes the electric-field effect, write down the corresponding PDEs from the biophysics, and nondimensionalize them. In Section 3, we present the effective, macroscale, homogenized PDE for electric potential. In Section 4, we present results from numerical simulations. In Section 5, we compare the homogenized system to the full system in terms of convenience and quality of approximation. In Appendix A, we present the measured, derived, and computational parameters that enter our model and simulations. Finally, in Appendix B, we present the derivation of the homogenized system.

## 2. The full model with electric-field coupling

We model cells as one-dimensional cables, each corresponding to a cylinder of radius  $r$  and length  $\ell$ . We consider only a monodomain by modeling extracellular space as grounded. We describe the electric potential inside cells through the cable equation

$$A\sigma_c \frac{\partial^2 \phi^i}{\partial x^2}(t, x) = S \left( C_m \frac{\partial \phi^i}{\partial t}(t, x) + I_{\text{ion}}(\phi^i(t, x), w_{\text{side}}^i(t, x)) \right) \quad \text{in } D^i, \quad (1)$$

where  $D^i = [i\ell, (i+1)\ell]$  is the domain of space occupied by the  $i$ th cell,  $\phi^i(t, x)$  is the intracellular potential within the  $i$ th cell,  $A = \pi r^2$  is the cross-sectional area of the cell,  $\sigma_c$  is the conductivity of the cytoplasm,  $S = 2\pi r$  is the perimeter of a cross section,  $C_m$  is the capacitance per unit area of membrane,  $I_{\text{ion}}$  is the outward ionic current per unit area of membrane, and  $w_{\text{side}}^i$  are the relevant gating variables along the lateral membrane of the  $i$ th cell. For ease of notation, we identify the domain of  $\phi^i$  with  $[0, \ell]$ . We shall also omit reference to gating variables  $w_{\text{side}}^i$  whenever convenient.

Resistors representing gap junctions allow current to flow directly between the interiors of adjacent cells. We model the cleft between cells as a single compartment with a

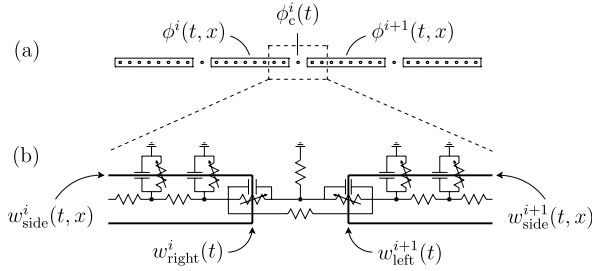


**Fig. 2** The geometry and circuit diagram for our full model of an electric-field mechanism in the presence of gap-junctional coupling. We describe cells as active cables coupled through direct resistive connections, and active membranes involving shared cleft potentials. We model extracellular space as grounded and ignore the effects of any changes in ion concentration. Panel (a) depicts the variables of electric potentials that occur in (1)–(4). Panel (b) depicts the gating variables. For clarity, the continuous domain inside cells is presented as if it were discrete. The diagram is not to scale, as the width of clefts is about three orders of magnitude smaller than the length of cells.

resistive connection to the grounded, extracellular space, which we refer to as the cleft-to-ground resistance. This choice of a one-compartment cleft potential is the primary structural difference between our model and that of Kucera et al. (2002). We model the ends of cells through active membranes by including the capacitive and ionic current from the cell ends into the cleft, see Fig. 2. Note that we ignore ion concentration changes throughout the model, and in particular within the clefts.

Current balance into the cleft provides the following equations for the cleft potential and boundary conditions for (1):

$$-A\sigma_c \frac{\partial \phi^i}{\partial x}(t, \ell) + A\sigma_c \frac{\partial \phi^{i+1}}{\partial x}(t, 0) = \frac{1}{R_c} \phi_c^i(t), \quad (2)$$

$$\begin{aligned} & -A\sigma_c \frac{\partial \phi^i}{\partial x}(t, \ell) - Ag_{\text{GJ, end}}(\phi^i(t, \ell) - \phi^{i+1}(t, 0)) \\ & = A \left( C_m \frac{\partial}{\partial t}(\phi^i(t, \ell) - \phi_c^i) + I_{\text{ion}}(\phi^i(t, \ell) - \phi_c^i(t), w_{\text{right}}^i(t)) \right), \quad (3) \end{aligned}$$

$$\begin{aligned} & A\sigma_c \frac{\partial \phi^{i+1}}{\partial x}(t, 0) + Ag_{\text{GJ, end}}(\phi^i(t, \ell) - \phi^{i+1}(t, 0)) \\ & = A \left( C_m \frac{\partial}{\partial t}(\phi^{i+1}(t, 0) - \phi_c^i) + I_{\text{ion}}(\phi^{i+1}(t, 0) - \phi_c^i(t), w_{\text{left}}^{i+1}(t)) \right), \quad (4) \end{aligned}$$

where  $R_c$  is the cleft-to-ground resistance,  $\phi_c^i$  is the potential of the cleft between the  $i$ th and  $i + 1$ -st cells,  $g_{\text{GJ, end}}$  is the conductance per unit area of the gap junctions, and  $w_{\text{left}}^i$  and  $w_{\text{right}}^i$  are gating variables for the left and right sides of the  $i$ th cell, respectively. Thus,  $w_{\text{right}}^i$  and  $w_{\text{left}}^{i+1}$  are the gating variables for the membranes facing the cleft between cells  $i$  and  $i + 1$ .

### 2.1. Nondimensionalization of the full system

As discussed in Neu and Krassowska (1993), significant variations of electric potential in a tissue occur on the length scale of the electrotonic length or space constant,  $\sqrt{R_m \sigma_c \ell}$ , where  $R_m$  is the sheet resistance of the cell membrane. That is,  $R_m^{-1}$  is a typical conductance per unit area of the cell membrane. We introduce the dimensionless variable  $\varepsilon = \sqrt{\frac{\ell}{R_m \sigma_c}}$  and rescale space so that the electrotonic length is unity. Cells then become of length  $\varepsilon$ . We also rescale time, potential, and current, as given by

$$\begin{aligned}\tilde{x} &= \frac{x}{\sqrt{R_m \sigma_c \ell}} = \frac{x}{\ell/\varepsilon}, & \tilde{t} &= \frac{t}{R_m C_m}, \quad \text{and} \\ \tilde{\phi} &= \frac{\phi}{\phi_{\text{typical}}}, & \tilde{I}_{\text{ion}} &= \frac{R_m}{\phi_{\text{typical}}} I_{\text{ion}}.\end{aligned}$$

We introduce the nondimensional parameters

$$\alpha = \frac{A}{S\ell}, \quad \beta = \varepsilon^2 \left( \frac{A\sigma_c}{\ell} \right) R_c, \quad \kappa = \varepsilon^2 g_{\text{GJ, end}} R_m,$$

where  $\alpha$  is a measure of the aspect ratio of cells,  $\beta$  is the nondimensionalized cleft-to-ground resistance, and  $\kappa$  is the nondimensionalized amount of gap junctional conductance between neighboring cells. The parameter  $\beta$  is a measure of the importance of cleft effects within the model. For example, if clefts were very wide,  $R_c$  and  $\beta$  would be very small, and there would be little distinction between the clefted and extracellular spaces. Thus,  $\beta = 0$  corresponds to a nonclefted model. Large  $\beta$  correspond to narrow, resistive clefts. We scale  $\beta$  and  $\kappa$  like  $\varepsilon^2$  because in this distinguished limit as  $\varepsilon \rightarrow 0$ , the homogenization procedure then gives finite yet nontrivial effects of clefts and gap junctions; see Appendix B.

Dropping the tildes, (1)–(4) become

$$\alpha \frac{\partial^2 \phi^i}{\partial x^2}(t, x) = \frac{\partial \phi^i}{\partial t}(t, x) + I_{\text{ion}}(\phi^i(t, x), w_{\text{side}}^i(t, x)), \quad (5)$$

$$\frac{\beta}{\varepsilon} \left( -\frac{\partial \phi^i}{\partial x}(t, \varepsilon) + \frac{\partial \phi^{i+1}}{\partial x}(t, 0) \right) = \phi_c^i, \quad (6)$$

$$\begin{aligned}-\frac{\partial \phi^i}{\partial x}(t, \varepsilon) - \frac{\kappa}{\varepsilon} (\phi^i(t, \varepsilon) - \phi^{i+1}(t, 0)) \\ = \varepsilon \left( \frac{\partial}{\partial t} (\phi^i(t, \varepsilon) - \phi_c^i(t)) + I_{\text{ion}}(\phi^i(t, \varepsilon) - \phi_c^i, w_{\text{right}}^i(t)) \right),\end{aligned} \quad (7)$$

$$\begin{aligned}\frac{\partial \phi^{i+1}}{\partial x}(t, 0) + \frac{\kappa}{\varepsilon} (\phi^i(t, \varepsilon) - \phi^{i+1}(t, 0)) \\ = \varepsilon \left( \frac{\partial}{\partial t} (\phi^{i+1}(t, 0) - \phi_c^i(t)) + I_{\text{ion}}(\phi^{i+1}(t, 0) - \phi_c^i, w_{\text{left}}^{i+1}(t)) \right).\end{aligned} \quad (8)$$

We subsequently refer to (5)–(8) as the full electric-field model, or as the full system.

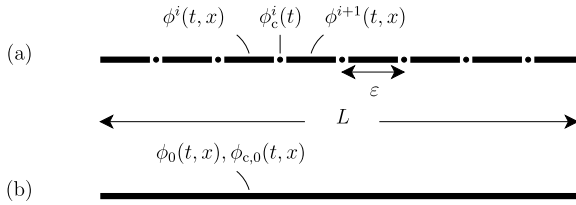


**Fig. 3** A schematic of the domains for the full (a) and homogenized (b) models. The full model is posed over discrete cells of length  $\varepsilon$  with a single-compartment cleft between adjacent cells. The intracellular potential within the  $i$ -th cell is  $\phi^i(t, x)$ , and the cleft potential to the right of the  $i$ -th cell is  $\phi_c^i(t)$ . Note that the cleft potential is defined only over a discrete set of points. The homogenized model is posed over the entire length  $L$  of tissue, as it does not resolve individual cells. The intracellular potential  $\phi_0(t, x)$  and the cleft potential  $\phi_{c,0}(t, x)$  are defined over the entire domain.

### 3. The homogenized model of electric-field coupling

We now perform homogenization to derive effective, macroscale evolution equations for the intracellular and cleft potentials. The index notation distinguishing the  $i$ th cell is cumbersome, and we introduce  $\phi(t, x)$  and  $w_{\text{side}}(t, x)$  as single functions defined over all space. We also introduce the functions  $\phi_c(t, x)$ ,  $w_{\text{left}}(t, x)$ , and  $w_{\text{right}}(t, x)$ , whose discrete samplings provide the cleft potentials and the gating variables for the left and right sides of cells. See Fig. 3 for a comparison of the domains of the full and homogenized systems.

We make the homogenization ansatz

$$\phi(t, x) = \phi_0(t, x) + \varepsilon\phi_1(t, x, x/\varepsilon) + \varepsilon^2\phi_2(t, x, x/\varepsilon) + O(\varepsilon^3). \tag{9}$$

Let  $y$  denote the third argument of  $\phi_1$  and  $\phi_2$ , which is known as the fast spatial variable. For cleft potentials, we assume  $\phi_c$  is a function of the slow variable  $x$ . That is,

$$\phi_c(t, x) = \phi_{c,0}(t, x) + O(\varepsilon), \tag{10}$$

where higher order terms in  $\varepsilon$  will not enter our derivation. Similarly, we assume that gating variables are only a function of time and of the slow spatial variable:

$$w_{\text{side}}(t, x) = w_{0,\text{side}}(t, x) + O(\varepsilon), \tag{11}$$

$$w_{\text{left}}(t, x) = w_{0,\text{end}}(t, x) + O(\varepsilon), \tag{12}$$

$$w_{\text{right}}(t, x) = w_{0,\text{end}}(t, x) + O(\varepsilon), \tag{13}$$

where  $w_{0,\text{side}}$  and  $w_{0,\text{end}}$  are defined by (11)–(13). Note in particular that the gating variables on the left and right ends of a cell are assumed to be equal. These assumptions of slow spatial variation in cleft potential and gating variables are strong and likely to be violated in the case of low gap junctional coupling. Nonetheless, they provide a starting point for mathematical analysis and could be relaxed in future work.

In Appendix B, we show that the effective equations satisfied by  $\phi_0(t, x)$ ,  $\phi_{c,0}(t, x)$ ,  $w_{0,\text{side}}(t, x)$ , and  $w_{0,\text{end}}(t, x)$  are

$$\begin{aligned} & \alpha \left( 1 - \frac{1}{1 + \kappa} \right) \frac{\partial^2 \phi_0}{\partial x^2} \\ & = \frac{\partial \phi_0}{\partial t} + I_{\text{ion}}(\phi_0, w_{0,\text{side}}) + 2\alpha \frac{\partial}{\partial t} (\phi_0 - \phi_{c,0}) + 2\alpha I_{\text{ion}}(\phi_0 - \phi_{c,0}, w_{0,\text{end}}), \end{aligned} \quad (14)$$

$$\phi_{c,0} = \beta \left( 2 \frac{\partial}{\partial t} (\phi_0 - \phi_{c,0}) + 2 I_{\text{ion}}(\phi_0 - \phi_{c,0}, w_{0,\text{end}}) \right). \quad (15)$$

We subsequently refer to (14)–(15) as the homogenized electric-field model, or as the homogenized system.

#### 4. Numerical simulation of the full and homogenized models

We now compare the full electric-field model to its homogenization via numerical simulation. We would like to replicate the effects of the electric-field mechanism reported in Kucera et al. (2002) and to determine the conditions under which the homogenized model accurately captures these effects. Specifically, we investigate the dependence of the conduction speed on the cleft-to-ground resistance, the degree of gap junctional coupling, and the degree of localization of  $\text{Na}^+$  channels to the intercalated disks. For physiological relevance, we investigate these questions using the Luo–Rudy 1991 ion channel dynamics (Luo and Rudy, 1991). There are more recent and accurate versions of this model (Faber and Rudy, 2000; Faber, 2008), but we use the Luo–Rudy 1991 dynamics because its relative simplicity.

Table A.1 presents the values of the nondimensional parameters that correspond to the physical parameters in the simulations from Kucera et al. (2002). As the value of  $\kappa$  corresponding to normal expression levels of gap junctions is almost unity, we may interpret  $\kappa$  as the fraction of gap junctions expressed relative to physiologically normal conditions. We run simulations for  $\kappa = 1$  to  $\kappa = 0.01$ .

To determine the effect of the  $\text{Na}^+$  channel distribution within a cell, we fix the total number of  $\text{Na}^+$  channels in a cell at its normal value, as per the Luo–Rudy 1991 dynamics, but distribute them in one of three ways: (i) 100% are located at the cell ends; (ii) 50% are at the ends; or (iii) the density is uniform. We denote the fraction of  $\text{Na}^+$  channels located at the cell ends as  $f_{\text{Na}}$ . These three cases correspond to  $f_{\text{Na}} = 1, 0.5$ , or  $\frac{2\alpha}{1+2\alpha}$ , respectively, where  $\alpha = 0.055$  is the ratio of the area of one end of a cell to the area on the sides of the cell. We refer to the last case as  $f_{\text{Na}} = \text{uniform}$ .

The last parameter we investigate is  $\beta$ , the nondimensional cleft-to-ground resistance. We run simulations from  $\beta = 10^{-4}$  to  $\beta = 5 \times 10^{-3}$ , which correspond to clefts of width 114 nm to 2 nm and to cleft-to-ground resistances of 0.52 M $\Omega$  to 26.1 M $\Omega$ . Appendix A details the relationship between cleft width and cleft-to-ground resistance. For ease of interpretation, we henceforth present cleft-to-ground resistance in dimensional units as  $R_c$  instead of  $\beta$ .

We define the front of a traveling action potential as the  $x$ -coordinate at which the potential crosses  $-40$  mV with  $\frac{d\phi}{dt} > 0$  and compute conduction velocity by finding the distance the front travels between specified times. These times are chosen such that the solution has already evolved into a traveling wave.

#### 4.1. Initial conditions and numerical scheme

In our numerical simulations, we consider an initial value problem over a domain of length  $L = 1.5225$ , which corresponds to a single file chain of 150 cells. In our model, we ignore the contribution to length of the clefts themselves because they are at least three orders of magnitude smaller than the length of cells. The domain corresponding to the first 10 cells is initially set so that the intracellular potential is at 0 mV. All cleft potentials are set to 0 mV. All remaining intracellular potentials and all gating variables are set at resting values. The exact initial value problems and their discretization can be found in Hand (2009).

The results presented in this paper were computed using Strang operator splitting, which we verified to be empirically second order in space and time. Specifically, we treated spatial derivatives implicitly with the Crank-Nicolson method, and we treated the ionic current and dynamics explicitly with a second order Runge-Kutta method. All linear systems that arose were solved via Gaussian elimination. Table A.1 provides specific values of the parameters used in the simulations. For both the full and homogenized models, the grid spacing corresponded to 10 nodes per cell.

#### 4.2. Numerical results for the full system

The solid lines in Fig. 4 show the conduction speeds given by the full electric-field model for selected values of the cleft-to-ground resistance, gap junctional coupling strength, and fraction of  $\text{Na}^+$  channels localized to the intercalated disks. Before we detail these effects, we remark on the apparent conduction failure for large cleft-to-ground resistance,  $R_c$ , in the top panel of Fig. 4. As  $R_c$  increases, the amplitude of the traveling wave decreases. Eventually it is low enough that it does not surpass our arbitrarily set threshold of  $-40$  mV. For example waveforms, see Fig. 5.

##### 4.2.1. Little effect of $\text{Na}^+$ channel localization on conduction speed with low cleft-to-ground resistance

We first remark on conduction speed for small cleft-to-ground resistance,  $R_c$ . Conduction speeds for  $R_c = 0.52 \text{ M}\Omega$  ( $\beta = 10^{-4}$ ,  $d_{\text{cleft}} = 114 \text{ nm}$ ) range from about 85 cm/s with normal gap junction levels to about 6 cm/s with 1% of normal gap junction expression levels. The conduction speeds are only weakly influenced by  $\text{Na}^+$  channel localization. This lack of dependence on  $f_{\text{Na}}$  is reasonable as the  $R_c \rightarrow 0$  limit corresponds to clefts that stay grounded, and hence act like extracellular space.

We remark that these values for conduction speed differ from those of Kucera et al. (2002). For example, the wavespeed in our model for normal levels of gap junctions and very wide clefts is 85 cm/sec. In the model of Kucera et al. (2002), it is 55 cm/sec. This quantitative discrepancy is most likely attributable to the different ionic current models of the studies. Our simulations used the 1991 version of the Luo–Rudy dynamics, whereas Kucera et al. (2002) used the more recent 2000 version (Faber and Rudy, 2000; Faber, 2008). One significant difference between these two versions is in the value of their maximal  $\text{Na}^+$  conductance. Simulations (not shown) reveal that this parameter alone accounts for about a third of the discrepancy in conduction speed. The rest of the discrepancy is likely a result of the many other differences in ionic current between the models.

##### 4.2.2. Little effect of cleft-to-ground resistance on conduction speed under uniform $\text{Na}^+$ channel density

The bottom panel of Fig. 4 shows that physiologically plausible cleft-to-ground resistances have little effect on conduction speed if  $\text{Na}^+$  channel density is uniform.

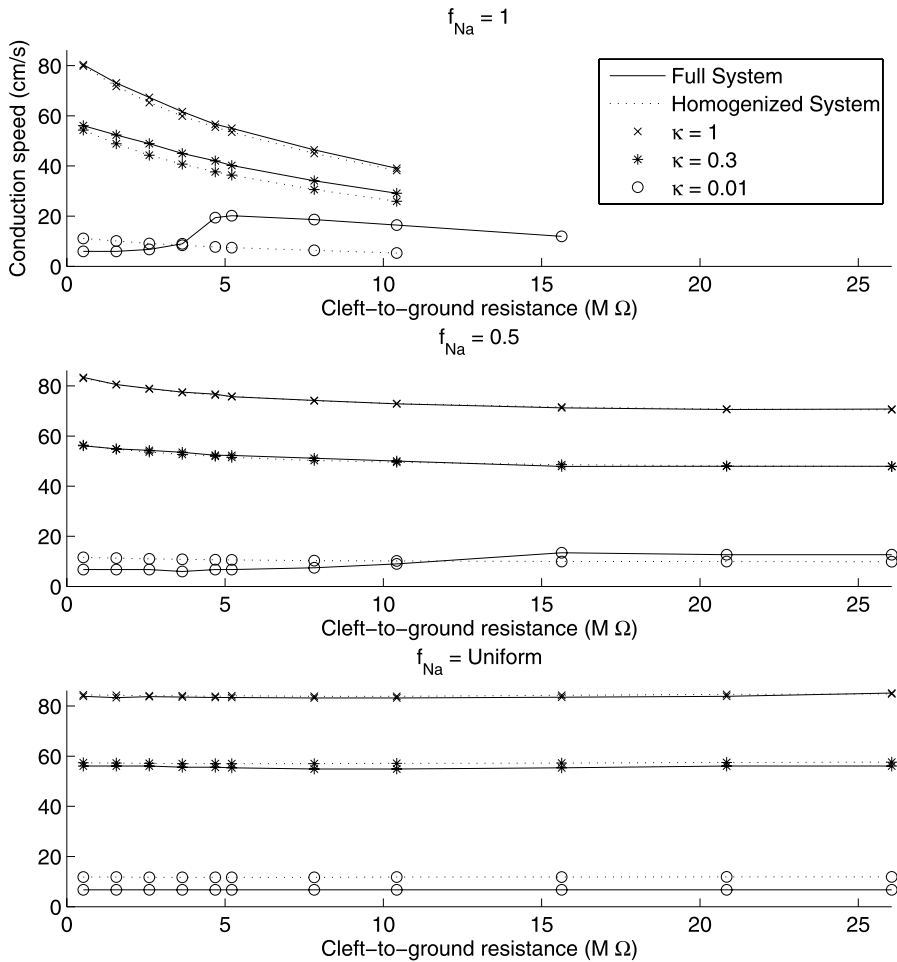


**Fig. 4** An overlay of the conduction speeds computed with the full and homogenized systems. At normal gap junction expression levels ( $\kappa = 1$ ) the systems agree well. Some quantitative disagreement is apparent even with 30% of normal levels ( $\kappa = 0.3$ ). The full and homogenized systems disagree even qualitatively when gap junctional coupling is reduced further ( $\kappa = 0.01$ ). Crosses, stars, and circles occur at values of  $R_c$  for which simulations were run, with 100%, 30%, and 1% gap junctional coupling, respectively.

#### 4.2.3. Reduced conduction speed with normal gap junctional coupling and localized $Na^+$ channels

As shown in the  $\kappa = 1$  curves in the top two panels of Fig. 4, conduction speed decreases monotonically over the range of  $R_c$  surveyed. With 100%  $Na^+$  channel localization, the clefts can act to slow down conduction by a third before propagation fails. With only 50%  $Na^+$  channel localization, the conduction speed decreases only slightly over the cleft-to-ground resistances investigated. These decreases in conduction velocity as a function of  $R_c$  are reasonable because the localization of  $Na^+$  channels to the intercalated disks forces  $Na^+$  current to go through the cleft-to-ground resistance.

#### 4.2.4. Enhanced conduction speed with low gap junctional coupling and localized $\text{Na}^+$ channels

As shown in the  $\kappa = 0.01$  curve in the top panel of Fig. 4, conduction speed is not necessarily monotonically decreasing in  $R_c$ . For example, the conduction speed with gap junctional coupling at 1% of normal is about 6 cm/s for  $R_c = 0.52 \text{ M}\Omega$  ( $\beta = 10^{-4}$ ,  $d_{\text{cleft}} = 114 \text{ nm}$ ), increasing to about 20 cm/s for  $R_c = 5.2 \text{ M}\Omega$  ( $\beta = 10^{-3}$ ,  $d_{\text{cleft}} = 11 \text{ nm}$ ), and then decreasing for larger cleft-to-ground resistances.

This nonmonotonicity of conduction speed as a function of cleft-to-ground resistance agrees with the corresponding qualitative result in Kucera et al. (2002). In that paper, the cleft width for maximal conduction speed under 1% of normal gap junction expression levels is  $d_{\text{cleft}} \approx 40 \text{ nm}$ . That maximal speed is  $\approx 15 \text{ cm/s}$ . These values are quantitatively different from ours, despite the qualitative agreement. We observe that the electric-field effect requires  $\text{Na}^+$  channel localization, as noted in Sperelakis and Mann (1977) and Picone et al. (1991).

#### 4.3. Numerical results for the homogenized system

The dotted lines in Fig. 4 show the conduction speed of the homogenized system for selected values of cleft-to-ground resistance, gap junctional coupling strength, and degree of  $\text{Na}^+$  channel localization to the intercalated disks. As with the full system, conduction speeds for small cleft-to-ground resistance are not strongly affected by  $\text{Na}^+$  channel localization. Also, the bottom panel of Fig. 4 shows that the physiologically plausible cleft-to-ground resistances have little effect on conduction speed when  $\text{Na}^+$  channel density is uniform. As shown in the  $\kappa = 1$  curves in the top two panels of Fig. 4, conduction speed decreases monotonically over the range of  $R_c$  surveyed. As with the full system, 100%  $\text{Na}^+$  channel localization can act to slow down conduction by a third.

##### 4.3.1. Reduced conduction speed with low gap junctional coupling and $\text{Na}^+$ channel localization

As shown in all the dotted lines in the top two panels of Fig. 4, conduction speed of the homogenized system is monotonically decreasing as a function of  $R_c$  for all gap junction expression levels. The simulations show no parameter range where more cleft resistance can increase conduction speed. This behavior is qualitatively different from that of the full system.

##### 4.3.2. Comparisons of the full and homogenized systems

Figure 4 overlays the conduction speeds of the full and homogenized systems for various values of gap junctional coupling, cleft-to-ground resistance, and  $\text{Na}^+$  channel localization. Figure 5 shows the electric potentials of the full and homogenized systems under high and low gap-junctional coupling, respectively. We observe good agreement between the models under full coupling, that is when  $\kappa = 1$ . The two systems do not agree very well under 1% coupling. Apparently, quantitative agreement between the two systems requires more than about 30% of normal coupling.

## 5. Discussion and conclusion

The intent of this paper is to provide a homogenized description of the electric-field mechanism or ephaptic effect in cardiac tissue for the ultimate purpose of easing

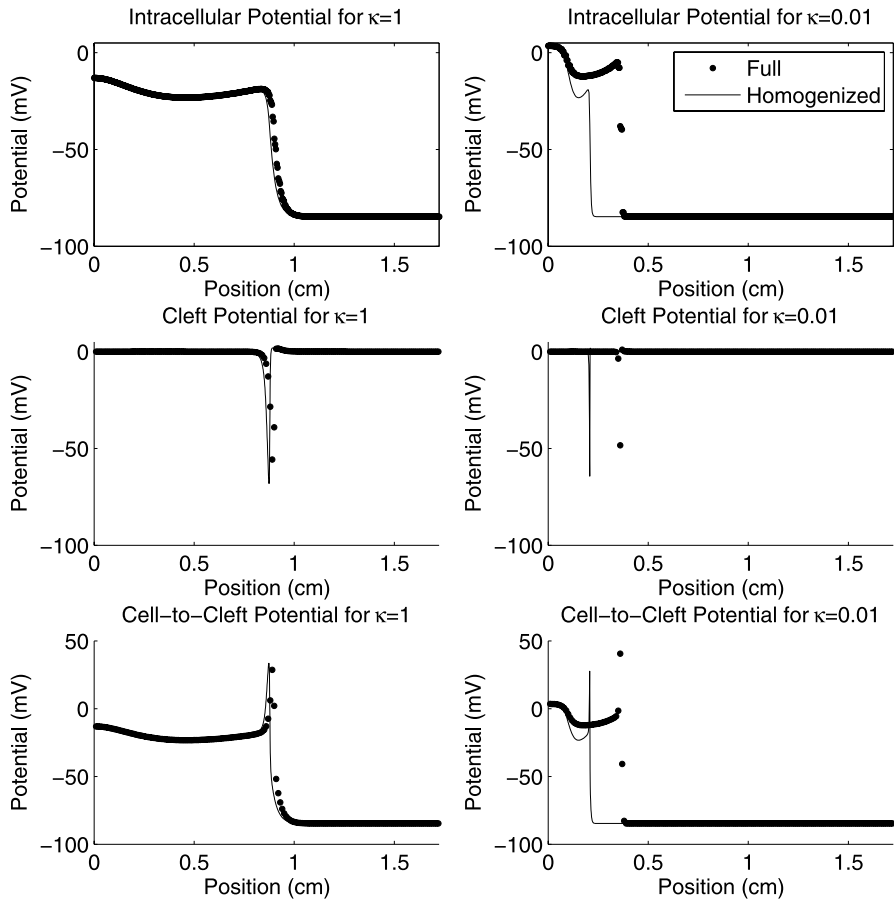


**Fig. 5** An overlay of the computed solutions to the full and homogenized systems with  $R_c = 5.2 \text{ M}\Omega$  ( $\beta = 10^{-3}$ ),  $\kappa = 1$ ,  $f_{\text{Na}} = 1$  for high ( $\kappa = 1$ ) and low ( $\kappa = 0.01$ ) gap-junctional coupling. The top panels show intracellular potentials. Note that individual cells can be resolved in the upstroke of the full simulations. The middle panels show cleft potentials, and the bottom panels show the cell-to-cleft potential differences. For clarity, the intracellular potentials of the full simulations are plotted for only a few of the 10 interior nodes. Note that the waveforms of the full and homogenized simulations are very similar under high gap junctional coupling. Under low gap-junctional coupling, the wave forms are markedly different. We remark that under this extreme of  $\text{Na}^+$  channel localization, intracellular potential itself does not demonstrate the spike and plateau typical of cardiac models. Instead, the cell-to-cleft transmembrane potentials exhibit the spike and plateau.

analysis and numerical simulations that delineate when that effect is relevant. To be most useful, such a description must be more convenient than, and capture the behavior of, the full description. We emphasize that the particular electric-field mechanism we explore does not include the effects of ion accumulation (Picone et al., 1991; Sperelakis and McConnell, 2002), which may be an important facilitator for conduction between cells.

### 5.1. *The homogenized system is more convenient than the full system*

One advantage of the homogenized system is the simplicity of its underlying geometry. For example, all potential and gating variables are defined at every spatial grid point. Further, there is no need to account individually for the boundary conditions at the ends of cells because the homogenization includes their effects automatically. Hence, numerical simulations become easier to code and analytical progress becomes more likely.

A second advantage is that the homogenized system requires less spatial resolution than the full system. Numerical experiments (not depicted) reveal that the wavespeeds computed from the homogenized equations with ten points per cell and one point per cell differ by less than 1%. We note that the coarse resolution of one point per cell would be meaningless for the full system because there would not be enough degrees of freedom to define the boundary fluxes. Hence, the linear systems involved in homogenized simulations are substantially smaller. Further, the only linear systems needing solution under a Strang splitting scheme arise from a standard diffusion equation, for which fast solution methods may be easy to find. These advantages in computational efficiency will become all the more important when the methodology of the present paper is scaled up to the three-dimensional case.

### 5.2. *The homogenized system captures the behavior of the full system under normal gap-junctional expression levels*

Our primary question is then does the homogenized system adequately capture the dynamics of the full system? We investigate this question empirically in the context of a realistic cardiac ionic current model.

Our simulations show that the homogenized system appears to capture the waveform and wavespeed of the full system when gap junctions are present at their normal levels. Note that the agreement between the homogenized model and the full model at normal gap-junctional coupling applies over the entire range of the parameter  $f_{\text{Na}}$ , which is the fraction of  $\text{Na}^+$  channels at the ends of cells. This parameter can have a substantial effect on the wavespeed, and that effect is captured by the homogenized model. It is important to note that a macroscale monodomain cable description cannot capture the effect because the parameter  $f_{\text{Na}}$  does not appear in such a model.

Unfortunately, the full and homogenized systems disagree when gap junction levels are significantly reduced. Hence, the homogenized equations in their present form are unlikely to contribute toward understanding cardiac propagation in gap junction deficient tissue. We especially remark on the extreme case of zero gap junctional coupling, that is,  $\kappa = 0$ . As repeatedly shown in the literature, conduction is possible in this case (Sperelakis and Mann, 1977; Kucera et al., 2002; Ramasamy and Sperelakis, 2007), but Eq. (14), of the homogenized system, does not allow traveling waves because the only  $x$ -dependent terms drop out.

Because the validity of the homogenized description does not depend on  $f_{\text{Na}}$ , the approximation quality of the homogenized model does not need to be checked whenever a new context, such as a species or pathology, is measured to give rise to a slightly different  $\text{Na}^+$  channel distribution.

We now conjecture why the homogenized and full systems disagree under low gap junctional coupling, yet agree under high coupling. Most likely, the discrepancy arises

because of a failure of the ansatz (10)–(13). The homogenized equations assume that gating variables and transmembrane potentials have  $O(1)$  variations only on the slow, macroscopic spatial scale. In particular, these variables on opposing sides of a cleft are assumed to be equal. The caricature of the electric-field mechanism shown in Fig. 1, however, suggests that there should be substantial differences in transmembrane potentials and gating variables across a cleft; see in particular Fig. 1b.

We suggest that the agreement of the full and homogenized systems under normal gap junction levels arises because the ansatz is met in that case. High gap-junctional coupling implies that potential differences between neighboring cells will result in large currents which erase these differences. This physical effect helps maintain the validity of the homogenization ansatz.

### 5.3. Comparison to existing homogenized models

We now compare our homogenized model to one that ignores cleft effects, as in typical bidomain models (Henriquez, 1993). The clefted model requires twice as much data storage because cleft potentials and gating variables are also computed for every grid point. Because of the convenient property that the spatial dependence term only occurs in the evolution equation (14) for  $\phi_0$ , the linear systems arising in our clefted, homogenized model are the same size as those for equivalent nonclefted models. All other terms can be treated explicitly under a Strang splitting scheme. Hence, our homogenized, clefted model is only marginally more expensive to use.

As initially observed in Sperelakis and Mann (1977), conduction via the electric-field mechanism requires that the ends of cells be more excitable than the sides of cells. Hence, it would be useful for homogenized models to have parameters that could distinguish between these two parts of the membrane. We remark that our homogenized electric-field model can conveniently account for differential  $\text{Na}^+$  densities between cell sides and ends. Current homogenized models, such as the bidomain equations, do not. Hence, our homogenized system is the starting point for a reasonable framework for teasing out the physiological effects due to the experimental observation of  $\text{Na}^+$  channel localization.

As mentioned above, this paper attempts to provide a homogenized model of the electric-field mechanism. While work remains to be done in extending the range of validity of the homogenization result, the derivation in this paper could be a starting point for further research involving more refined ansatzes. Additionally, we believe that the homogenized model in its present form may still be useful in cardiac electrophysiology because it captures the effects of cleft-to-ground resistance and  $\text{Na}^+$  channel localization on action potential propagation in tissue with normal gap-junctional coupling.

### Acknowledgements

We are indebted to Boyce Griffith for helpful discussions. P.H. was partially supported by the United States Department of Defense through a National Defense Science and Engineering Graduate Fellowship, a New York University Dean's Dissertation Fellowship, and a Whitehead Foundation Junior Faculty Fellowship awarded to Boyce Griffith. We would like to thank several anonymous reviewers for substantially improving this work.

**Table A.1** The measurable, derived, and simulation parameters that enter our full and homogenized models

Measurable parameters			
Symbol	Parameter	Value	Reference
$r$	Radius of cell	$11 \times 10^{-4}$ cm	(Kucera et al., 2002)
$\ell$	Length of cell	$10^{-2}$ cm	(Kucera et al., 2002)
$\sigma_c$	Cytosolic conductivity	$6.67$ mS cm $^{-1}$	(Kucera et al., 2002)
$\sigma_{\text{ext}}$	Extracellular conductivity	$6.67$ mS cm $^{-1}$	(Kucera et al., 2002)
$g_{\text{GJ,end}}$	Gap junctional conductance per area	$6.66 \times 10^2$ mS cm $^{-2}$	(Kucera et al., 2002)
$R_m$	Membrane sheet resistance	$20$ k $\Omega$ cm $^2$	(Neu and Krassowska, 1993)
$C_m$	Membrane capacitance per area	$1$ $\mu$ F cm $^{-2}$	(Kucera et al., 2002)
$d_{\text{cleft}}$	Cleft width	2–115 nm	
Derived parameters			
Symbol	Parameter	Value	Expression
$R_c$	Cleft-to-ground resistance	$2.98 \times 10^4$ k $\Omega$ $-5.19 \times 10^2$ k $\Omega$	$\frac{1}{8\pi\sigma_{\text{ext}}d_{\text{cleft}}}$
$\alpha$	Aspect ratio of cells	0.055	$\frac{\pi r^2}{2\pi r\ell}$
$\varepsilon$	Nondimensional length of cells	0.0087	$\sqrt{\frac{\ell}{R_m\sigma_c}}$
$\kappa$	Nondimensional gap junctional conductivity	0.9985	$\varepsilon^2 g_{\text{GJ,end}} R_m$
$\beta$	Nondimensional cleft resistance	$5.7 \times 10^{-3}$ – $10^{-4}$	$\varepsilon^2 \pi r^2 \frac{\sigma_c}{\ell} R_c$
Simulation parameters			
Symbol	Parameter	Value (nondim)	Value
$\Delta t$	Time step	$1 \times 10^{-4}$	$2 \times 10^{-3}$ ms
$\Delta x$	Node spacing	$8.7 \times 10^{-4}$	$1 \times 10^{-3}$ cm
$L$	Domain length	1.5225	1.75 cm

## Appendix A: Simulation parameters

We run the simulations of the full and homogenized systems with nondimensional parameters corresponding to the dimensional values used in Kucera et al. (2002). The cleft-to-ground resistance in the models would be very difficult to measure experimentally. As in Kucera et al. (2002), we instead relate it to the cleft width through  $R_c = \frac{1}{8\pi\sigma_{\text{ext}}d_{\text{cleft}}}$ , where  $d_{\text{cleft}}$  is the cleft width and  $\sigma_{\text{ext}}$  is the conductivity of extracellular space. This formula can be derived by computing the average cleft potential of the solution to Laplace's equation over the cleft, subject to uniform current flow into its sides. Plausible values for  $d_{\text{cleft}}$  are on the order of 10–100 nm.

## Appendix B: Derivation of homogenized system

We now derive the effective equations (14)–(15) from the nondimensionalized, full system (5)–(8) and the ansatzes (9)–(13).

Applying the ansatz (9) to the PDE (5), (7), (8) and extracting the leading terms, of order  $\varepsilon^{-1}$ , we obtain

$$\begin{aligned} \frac{\partial^2 \phi_1}{\partial y^2}(t, x, y) &= 0 \quad \text{in } [0, 1], \\ -\frac{\partial \phi_1}{\partial y}(t, x, 1) - \kappa(\phi_1(t, x, 1) - \phi_1(t, x, 0)) &= -\frac{\partial \phi_0}{\partial x}(t, x), \\ \frac{\partial \phi_1}{\partial y}(t, x, 0) + \kappa(\phi_1(t, x, 1) - \phi_1(t, x, 0)) &= \frac{\partial \phi_0}{\partial x}(t, x). \end{aligned}$$

Solving, we obtain

$$\phi_1(t, x, y) = \frac{1}{1 + \kappa} \left( \frac{1}{2} - y \right) \frac{\partial \phi_0}{\partial x}(t, x). \quad (\text{B.1})$$

The next terms, of order  $\varepsilon^0$ , are

$$\begin{aligned} \alpha \left( \frac{\partial^2 \phi_0}{\partial x^2}(t, x) + 2 \frac{\partial^2 \phi_1}{\partial x \partial y}(t, x, y) + \frac{\partial^2 \phi_2}{\partial y^2}(t, x, y) \right) \\ = \frac{\partial \phi_0}{\partial t}(t, x) + I_{\text{ion}}(\phi_0(t, x), w_{0,\text{side}}(t, x)), \end{aligned} \quad (\text{B.2})$$

$$\begin{aligned} -\frac{\partial \phi_2}{\partial y}(t, x, 1) - \kappa(\phi_2(t, x, 1) - \phi_2(t, x, 0)) \\ = \frac{\partial \phi_1}{\partial x}(t, x, 1) + \frac{\partial}{\partial t}(\phi_0(t, x) - \phi_{c,0}) + I_{\text{ion}}(\phi_0(t, x) - \phi_{c,0}(t, x), w_{0,\text{end}}(t, x)), \end{aligned} \quad (\text{B.3})$$

$$\begin{aligned} \frac{\partial \phi_2}{\partial y}(t, x, 0) + \kappa(\phi_2(t, x, 1) - \phi_2(t, x, 0)) \\ = -\frac{\partial \phi_1}{\partial x}(t, x, 0) + \frac{\partial}{\partial t}(\phi_0(t, x) - \phi_{c,0}) + I_{\text{ion}}(\phi_0(t, x) - \phi_{c,0}(t, x), w_{0,\text{end}}(t, x)). \end{aligned} \quad (\text{B.4})$$

The solvability condition for  $\phi_2$  provides the effective dynamics for  $\phi_0$ . We obtain it by integrating the differential equation (B.2) from  $y = 0$  to  $y = 1$ , giving

$$\alpha \frac{\partial^2 \phi_0}{\partial x^2} + 2\alpha \frac{\partial \phi_1}{\partial x} \Big|_{y=0}^{y=1} + \alpha \frac{\partial \phi_2}{\partial y}(t, x, y) \Big|_{y=0}^{y=1} = \frac{\partial \phi_0}{\partial t}(t, x) + I_{\text{ion}}(\phi_0(t, x), w_{0,\text{side}}(t, x)). \quad (\text{B.5})$$

From the boundary conditions (B.3)–(B.4), we observe

$$\begin{aligned} \frac{\partial \phi_2}{\partial y}(t, x, y) \Big|_{y=0}^{y=1} &= -\frac{\partial \phi_1}{\partial x}(t, x, 1) + \frac{\partial \phi_1}{\partial x}(t, x, 0) \\ &\quad - 2 \frac{\partial}{\partial t}(\phi_0(t, x) - \phi_{c,0}(t, x)) \\ &\quad - 2 I_{\text{ion}}(\phi_0(t, x) - \phi_{c,0}(t, x), w_{0,\text{end}}(t, x)) \end{aligned} \quad (\text{B.6})$$

$$\begin{aligned}
&= \frac{1}{1+\kappa} \frac{\partial^2 \phi_0}{\partial x^2} - 2 \frac{\partial}{\partial t} (\phi_0(t, x) - \phi_{c,0}(t, x)) \\
&\quad - 2I_{\text{ion}}(\phi_0(t, x) - \phi_{c,0}(t, x), w_{0,\text{end}}(t, x)).
\end{aligned} \tag{B.7}$$

To get the homogenized equation (14) for the dynamics of  $\phi_0$ , we combine (B.5), (B.1), and (B.7).

All that remains is to obtain the governing equation for  $\phi_{c,0}$ .

Plugging the ansatz (9) into (6) and extracting the leading order terms, of size,  $\varepsilon^0$ , we obtain

$$\beta \left( -\frac{\partial \phi_1}{\partial x}(t, x, 1) + \frac{\partial \phi_1}{\partial x}(t, x, 0) - \frac{\partial \phi_2}{\partial y}(t, x, 1) + \frac{\partial \phi_2}{\partial y}(t, x, 0) \right) = \phi_{c,0}(t, x) \tag{B.8}$$

Applying (B.1) and (B.7), this equation simplifies to (15), which indicates a nontrivial contribution of the clefts to the dynamics. We remark that the scaling of  $\beta$  like  $\varepsilon^2$ , was crucial in the derivation of (B.8). Had  $\beta$  been scaled like  $\varepsilon$ , the equivalent of (B.8) would be  $\phi_{c,0}(t, x) = 0$ .

## References

- Copene, E., Keener, J., 2008. Ephaptic coupling of cardiac cells through the junctional electric potential. *J. Math. Biol.* 57(2), 265–284.
- Evans, L., 2002. *Partial Differential Equations*. American Mathematical Society, Providence, pp. 218–221.
- Faber, G., 2008. Cardiac Bioelectricity Research and Training Center (CBRTC). The Luo-Rudy dynamic (LRd) model of the mammalian ventricular action potential. Available at: <http://www.cwru.edu/med/CBRTC/LRdOnline/>. Accessed December 2008
- Faber, G., Rudy, Y., 2000. Action potential and contractility changes in  $[\text{Na}^+]_i$  overloaded cardiac myocytes: a simulation study. *Biophys. J.* 78, 2392–2404.
- Gutstein, D., Morley, G., Tamaddon, H., Vaidya, D., Schneider, M., Chen, J., Chien, K., Stuhlmann, H., Fishman, G., 2001. Conduction slowing and sudden arrhythmic death in mice with cardiac-restricted inactivation of connexin43. *Circ. Res.* 88, 333–339.
- Hand, P., 2009. Homogenization in cardiac electrophysiology and blow-up in bacterial chemotaxis. Doctoral dissertation. New York University, New York.
- Henriquez, C., 1993. Simulating the electrical behavior of cardiac tissue using the bidomain model. *Crit. Rev. Biomed. Eng.* 21, 1–77.
- Hornung, U., 1997. *Homogenization and Porous Media*. Springer, New York.
- Kucera, J., Rorh, S., Rudy, Y., 2002. Localization of sodium channels in intercalated disks modulates cardiac conduction. *Circ. Res.* 91, 1176–1182.
- Luo, C., Rudy, Y., 1991. A model of the ventricular cardiac action potential. Depolarization, repolarization, and their interaction. *Circ. Res.* 68, 1501–1526.
- Mori, Y., Fishman, G., Peskin, C., 2008. Ephaptic conduction in a cardiac strand model with 3D electrodiffusion. *Proc. Nat. Acad. Sci.* 105, 6463–6468.
- Neu, J., Krassowska, W., 1993. Homogenization of syncytial tissues. *Crit. Rev. Biomed. Eng.* 21, 137–199.
- Picone, J., Sperelakis, N., Mann, J., 1991. Expanded model of the electric field hypothesis for propagation in cardiac muscle. *Math. Comput. Model.* 15(8), 13–35.
- Ramasamy, L., Sperelakis, N., 2007. Cable properties and propagation velocity in a long single chain of simulated myocardial cells. *Theor. Biol. Med. Model.* 4, 36.

- 
- Rohr, S., 2004. Role of gap junctions in the propagation of the cardiac action potential. *Cardiovasc. Res.* 62, 309–322.
- Sperelakis, N., Mann, J., 1977. Evaluation of electric field changes in the cleft between excitable cells. *J. Theor. Biol.* 64, 71–96.
- Sperelakis, N., McConnell, K., 2002. Electric field interactions between closely abutting excitable cells. *IEEE Eng. Med. Biol. Mag.* 21, 77–89.